Supplementary Information (SI) for Energy & Environmental Science.

Supporting Information for:

Effective Mass Model for Thermoelectrics

Minsu Heo,‡[ab] Kyu Hyoung Lee,‡[c] Junwoo Song,‡[d] Changwoo Lee,[b] Insub Lee,[d] Kwangjoo Kim,[d] Hoon Wee,[d] Joonhyun Lee,[d] Youngdeog Koh,*[d] Hyun-Sik Kim,*[b] and G. Jeffrey Snyder*[a]

[a]Department of Materials Science and Engineering, Northwestern University, Evanston 60208, IL, United States.

[b]Department of Materials Science and Engineering, University of Seoul, Seoul 02504, Republic of Korea.

[c]Department of Materials Science and Engineering, Yonsei University, Seoul 03722, Republic of Korea.

[d]Samsung Research, Samsung Electronics, Seoul 06765, Republic of Korea.

‡These authors contributed equally to this work

*Correspondence to: yd.koh@samsung.com (Y. Koh), hyunsik.kim@uos.ac.kr (H.-S. Kim), jeff.snyder@northwestern.edu (G. J. Snyder)

The file includes

Sections S1 to S4

Figures S1 to S7

Tables S1 to S6

Section S1. Effective Mass (EM) model

The effective mass (EM) model is used to independently extract the Seebeck effective mass (m_S^*) and the nondegenerate mobility (μ_0) by fitting the Hall carrier concentration (n_{H})-dependent Seebeck coefficient (S) and Hall mobility (μ_{H}) using the following relations (fig. S1A):

$$S = \frac{k_B}{e}\left(\frac{2F_1(\eta)}{F_0(\eta)} - \eta\right) \tag{S1}$$

$$\mu_H = \mu_0 \frac{F_{-1/2}(\eta)}{2F_0(\eta)} \tag{S2}$$

$$n_H = \frac{16\pi}{3}\left(\frac{2m_S^* k_B T}{h^2}\right)^{3/2} \frac{\left(F_0(\eta)\right)^2}{F_{-1/2}(\eta)} \tag{S3}$$

$$F_i(\eta) = \int_0^\infty \frac{\varepsilon^i}{1 + \exp\left(\varepsilon - \eta\right)} d\varepsilon \tag{S4}$$

where, k_B, e, $F_i(\eta)$, and η are the Boltzmann constant, electric charge, Fermi integral of order I and the reduced chemical potential, respectively.[1] By varying η over a typical range from -10 to 10, n_{H}-dependent electrical conductivity (σ) and power factor ($S^2\sigma$) can be determined using eqs. S2-S4 (fig. S1A):

$$\sigma = n_H e \mu_H = \mu_0 \frac{8\pi e}{3}\left(\frac{2m_S^* k_B T}{h^2}\right)^{3/2} F_0(\eta) \tag{S5}$$

$$PF = \mu_0 m_S^{*\,3/2} \frac{8\pi k_B^2}{3e^2}\left(\frac{2k_B T}{h^2}\right)^{3/2} F_0(\eta)\left(\frac{2F_1(\eta)}{F_0(\eta)} - \eta\right)^2 \tag{S6}$$

In eq. S6, the $\mu_0 \times (m_S^*/m_e)^{3/2}$ represents the weighted mobility (μ_{w}), a key band parameter governing the theoretical maximum $S^2\sigma$. The electronic contribution to thermal conductivity (κ_e) is calculated via the Wiedemann–Franz law:

$$\kappa_e = L\sigma T \tag{S7}$$

The Lorenz factor (L) in the EM model is given by:

$$L = \left(\frac{k_B}{e}\right)^2 \frac{3F_0(\eta)F_2(\eta) - 4F_1^2(\eta)}{F_0^2(\eta)} \tag{S8}$$

Substituting eq. S5 and eq. S8 into eq. S7 yields:

$$\kappa_e = \frac{8\pi\mu_0\kappa_B^2 T}{3e}\left(\frac{2m_S^* k_B T}{h^2}\right)^{3/2} \frac{3F_0(\eta)F_2(\eta) - 4F_1^2(\eta)}{F_0(\eta)} \tag{S9}$$

The lattice thermal conductivity (κ_{L}) is extracted by subtracting κ_e from the experimentally measured total thermal conductivity (κ). The dimensionless thermoelectric figure-of-merit zT is then estimated as:

$$zT = \frac{S^2\sigma T}{\kappa_e + \kappa_L} \tag{S10}$$

The thermoelectric quality factor (B) is defined as:

$$B = 0.674\left(\frac{T}{300\ K}\right)^{5/2}\frac{\left(\frac{\mu_w}{1000\ cm^2\ V^{-1}\ s^{-1}}\right)}{\left(\frac{\kappa_L}{W\ m^{-1}\ K^{-1}}\right)} \qquad \text{(S11)}$$

Finally, eq. S10 can be reformulated by combining eqs. S1, S5, and S9 to yield zT in terms of the B and η:

$$zT = \frac{\left(\frac{2F_1(\eta)}{F_0(\eta)} - \eta\right)^2 BF_0(\eta)}{1 + \left[\frac{3F_2(\eta)}{F_0(\eta)} - \left(\frac{2F_1(\eta)}{F_0(\eta)}\right)^2\right] BF_0(\eta)} \qquad \text{(S12)}$$

By plotting zT from eq. S12 against n_H from eq. S3, the theoretical maximum zT and corresponding optimal carrier concentration can be determined, governed by the material's intrinsic B (fig. S1B).

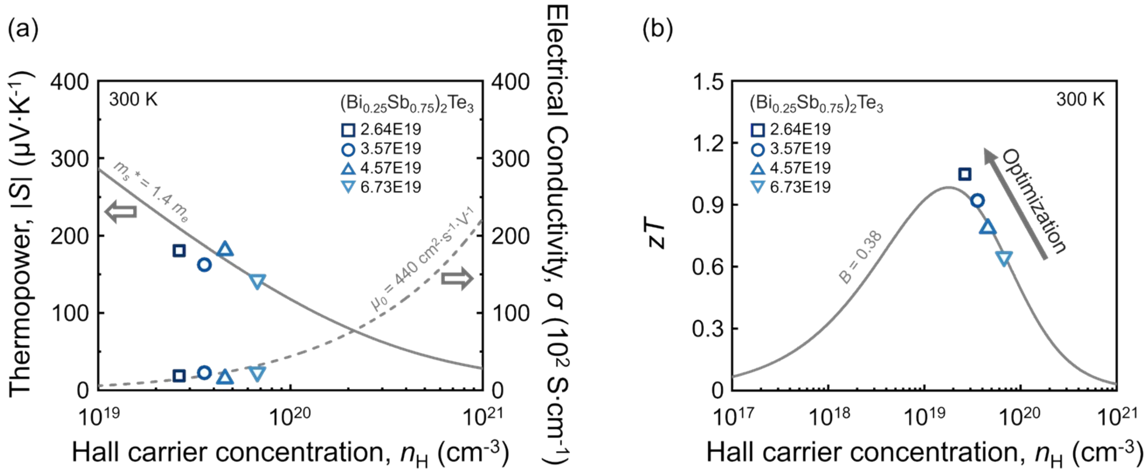

Fig. S1. Application of the Effective Mass (EM) model. (a) Estimation of the Seebeck effective mass (m_S^*) and nondegenerate mobility (μ_0). (b) Calculated maximum thermoelectric figure-of-merit (zT) and corresponding optimum Hall carrier concentration (n_H) for *p*-type $(Bi_{0.25}Sb_{0.75})_2Te_3$.[2]

Theoretical maximum zT as a function of thermoelectric quality factor (B)

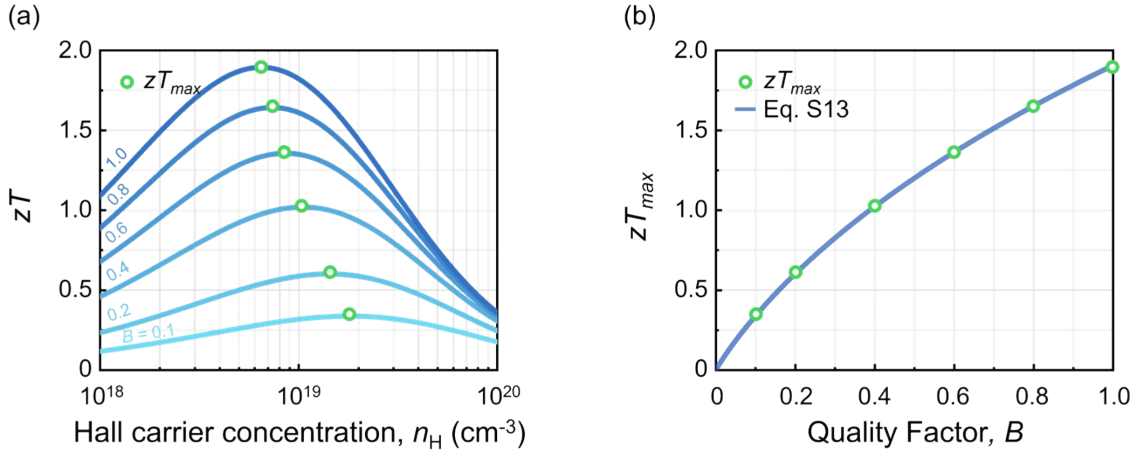

Fig. S2. Thermoelectric quality factor (B) determines the theoretical maximum thermoelectric figure-of-merit (zT_{max}). (a) thermoelectric figure-of-merit (zT) as a function of Hall carrier concentration (n_H), calculated using the EM model for various Bs. The corresponding zT_{max} values are indicated by green circles. (b) Green circles from (a) are mapped onto a B-zT_{max} plot, with the solid curve representing the theoretical relationship derived from eq. S13.

In fig. S2(a), n_H-dependent zT was calculated based on the EM model, with the B varied from 0.1 to 1.0. From this dataset, the theoretical maximum zT (zT_{max}) achievable through carrier concentration optimization was determined for each Bs. Using these B-dependent zT_{max}, the relationship between the corresponding B and zT_{max} is derived as:

$$zT_{max} = \frac{B}{0.232 + \left(0.293 \times B^{2/3}\right)} \qquad \text{(S13)}$$

The error between the zT_{max} calculated using EM model and eq. S13 for the same B was less than 0.5%.

Section S2. Calculation of weighted mobility (μ_w) from experimental |*S*| and σ of $(Bi_{0.25}Sb_{0.75})_2Te_3$

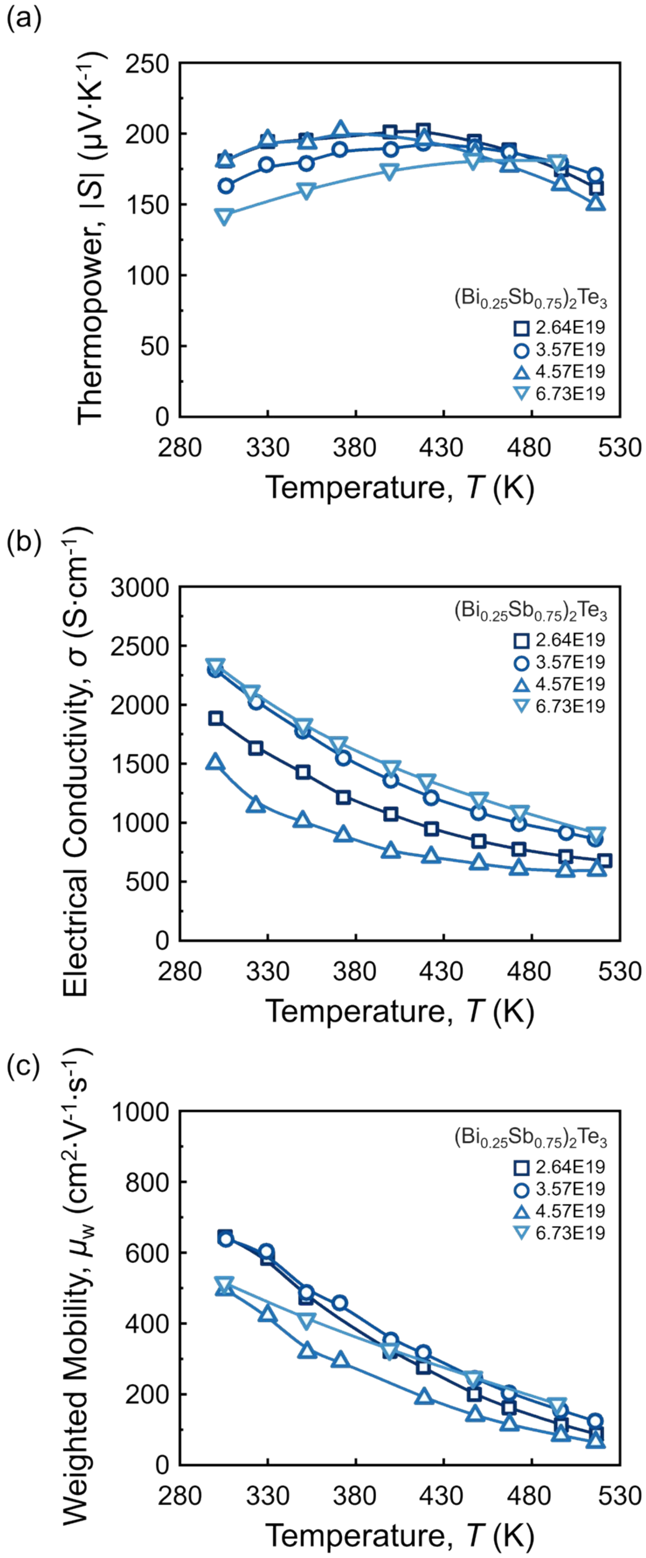

Fig. S3. Calculation of weighted mobility (μ_w) from experimental thermopower (|*S*|) and electrical conductivity (σ). Temperature-dependent (a) |*S*|, (b) σ, and (c) μ_w of *p*-type $(Bi_{0.25}Sb_{0.75})_2Te_3$.[2]

The analytical form used to calculate the weighted mobility, μ_w (Eq. 5), is a closed-form approximation to the Drude-Sommerfeld free-electron (parabolic band with effective mass) solution and reproduces the exact result within ~3% for $|S| > 20$ μV K^{-1}, smoothly interpolating between the degenerate and non-degenerate limits. Importantly, μ_w is obtained directly from measured $|S|$ and σ without requiring explicit Hall measurements or explicitly assuming the Single Parabolic Band (SPB) model; deviations from ideal free-electron trends are reflected as measurable variations in the extracted descriptor.

The physical interpretation of the extracted parameters is most robust when diffusion thermopower dominates and $|S|$ varies monotonically with carrier concentration. Caution is therefore required at low temperatures (typically below ~100 K in most thermoelectric semiconductors) where phonon drag significantly modifies $|S|$, or at elevated temperatures where bipolar excitation becomes appreciable, reducing the net thermopower. For example, in narrow-gap systems such as Bi_2Te_3-based materials (band gap (E_g) ~ 0.15 eV), bipolar effects may become appreciable above 450 K. In intermediate-gap materials such as PbTe (E_g ~ 0.3 eV), bipolar contributions typically emerge near 600 K. For wider band gap thermoelectrics ($E_g \geq 0.5$ eV), bipolar effects are generally negligible below 800-1000 K.

Eq. (6), being algebraically derived from Eq. (5), inherits the same applicability range. For Eq. (7), additional considerations arise because both μ_w and thermal conductivity are involved. Bipolar thermal conductivity is not explicitly included in the closed-form zT formulation; while bipolar effects can indirectly influence the estimate through the measured $|S|$, the additional heat transport associated with minority-carrier diffusion is not included. The electronic thermal conductivity is estimated using a Lorenz number based on the SPB model approximation, which is accurate for $|S| > 20$ μV K^{-1}. For systems with significant band non-parabolicity, scattering mechanisms beyond acoustic phonon scattering, or multiple band contributions, the Lorenz number may deviate from the SPB model-based expression by up to ~25%. Nevertheless, because the uncertainty associated with μ_w remains within ~3%, the propagated uncertainty in the calculated zT near optimal doping is typically reduced to ~10-15%, comparable to common experimental uncertainties in thermoelectric measurements.

Overall, the zT expression (Eq. 7) is applicable across both degenerate and moderately non-degenerate semiconducting thermoelectrics in which $|S|$ serves as a monotonic proxy for the reduced Fermi level and diffusion thermopower dominates the transport response. While the formulation originates from a near-parabolic free-electron treatment, it is employed here as an effective transport descriptor and does not require strictly SPB model behavior; in systems with multi-band contributions or moderate band non-parabolicity, the extracted quantities should be interpreted as effective parameters representing the dominant transport channel. Eq. 7 is therefore most reliable in regimes where bipolar excitation remains limited and band-like carrier transport governs both electrical and thermal responses. Outside these conditions, especially in strongly compensated and narrow-gap systems operating at elevated temperatures, the calculated zT should be interpreted as a descriptor-level estimate rather than a quantitatively rigorous prediction.

Section S3. Predictions of zT_{max} and optimum $|S|$ from temperature-dependent S, σ, and κ in Mg_3Sb_2

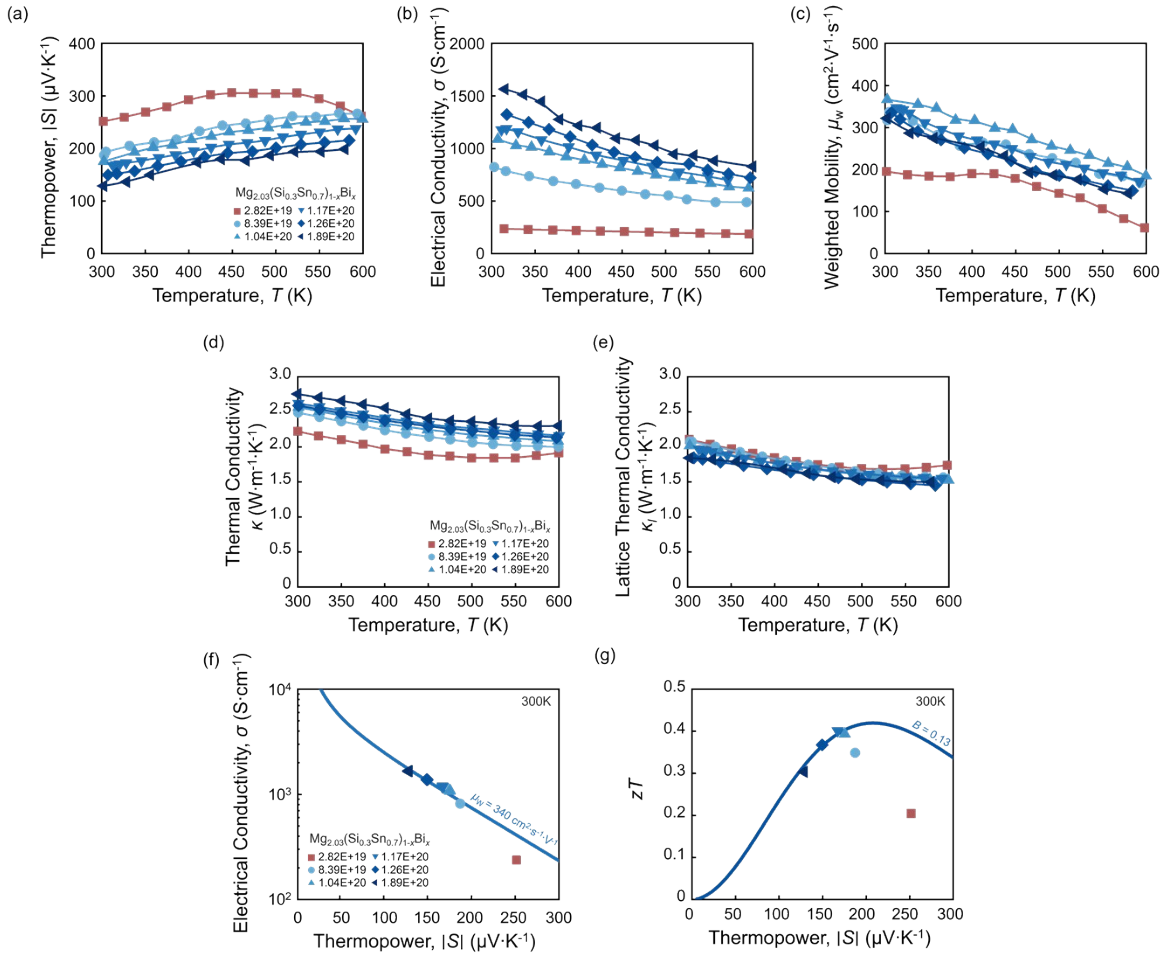

Fig. S4. Application of Eqs. 6 and 7 to Bi-doped $Mg_2Si_{0.3}Sn_{0.7}$. Temperature-dependent (a) thermopower ($|S|$), (b) electrical conductivity (σ), (d) thermal conductivity (κ) measurements. Estimation of (c) weighted mobility (μ_w), (e) lattice thermal conductivity (κ_L), (f) $|S|$-dependent σ, and (g) calculated zT and corresponding $|S|$ for Bi-doped $Mg_2Si_{0.3}Sn_{0.7}$.[3]

Fig. S4 outlines a systematic approach for evaluating material engineering strategies and predicting the zT_{max} and corresponding optimal $|S|$ without relying on Hall measurements or complex calculations. As a representative case, Bi-doped $Mg_2Si_{0.3}Sn_{0.7}$ is analyzed.[3] The temperature-dependent $|S|$ and σ of the least-doped sample (shown in red) and heavily Bi-doped samples (in blue) are presented in figs. S4(a) and S4(b). As Bi doping content increases, $|S|$ decreases and σ increases, consistent with conventional carrier concentration tuning. However, this observation alone does not reveal any anomalous transport behavior.

To further assess the impact of doping, the μ_w was calculated from experimental $|S|$ and σ using Eq. 5. As shown in fig. S4(c), the least-doped sample exhibits a distinctly different temperature-dependent μ_w compared to the heavily doped counterparts. The relatively constant μ_w up to ~430 K suggests a different dominant carrier scattering mechanism in the low-doping regime.

To evaluate the effect of doping on phonon transport, κ_L was extracted by subtracting the electronic thermal conductivity ($\kappa_e = L(|S|)\sigma T$, where L is the Lorenz number as a function of $|S|$) from the measured total thermal conductivity (κ) (fig. S4(d) and fig. S5(a)). Although heavily doped samples show higher κ, their κ_L values remain comparable to that of the least-doped sample (Fig. S4(e)). This similarity becomes more evident at 300 K, where bipolar conduction is negligible. Plotting κ against κ_e (fig. S5(b)), the y-intercept of a unit-slope line corresponds to κ_L. The alignment of all data points, regardless of doping level, with this line indicates that Bi doping has minimal effect on κ_L.

Focusing on transport behavior at 300 K, experimental $|S|$ and σ were extracted from figs. S4(a) and S4(b) and mapped onto $|S|$-σ space in fig. S4(f). A theoretical $|S|$-dependent σ curve was calculated using Eq. 6 and fitted to the data by adjusting μ_w (table S1). While all heavily doped samples are well described by a single μ_w value of 340 cm^2 V^{-1} s^{-1}, the least-doped sample deviates significantly from this curve. The resulting $|S|$-σ trend confirms that initial Bi doping enhances μ_w, but further doping primarily increases carrier concentration without improving μ_w, resulting in no further improvement in the theoretical maximum $S^2\sigma$ (fig. S6).

Finally, the symbols in fig. S4(g) show the experimentally measured zT values plotted as a function of $|S|$. The B was fitted to the data by comparing experimental results to theoretical $|S|$-zT curve calculated using Eq. 7 (table S2). For heavily Bi-doped samples, $B \sim 0.13$ effectively reproduces the experimental zT trend. Among these samples, increased Bi doping leads to reduced $|S|$ without further enhancement in B, thus lowering zT. Optimization of $|S|$ to ~205 μV K^{-1} while maintaining the same B yields a maximum zT of approximately 0.42 at 300 K. This analysis confirms that the observed zT enhancement is primarily attributed to the improved μ_w achieved through Bi doping. Importantly, the accuracy of the Eq. 7 was compared against the EM model. Across a broad range of B values (0.1 to 1.5), the maximum deviation in calculated zT at a given $|S|$ remained below 3.6%, demonstrating that Eq. 7 provides a highly reliable tool for evaluating thermoelectric performance (fig. S7).

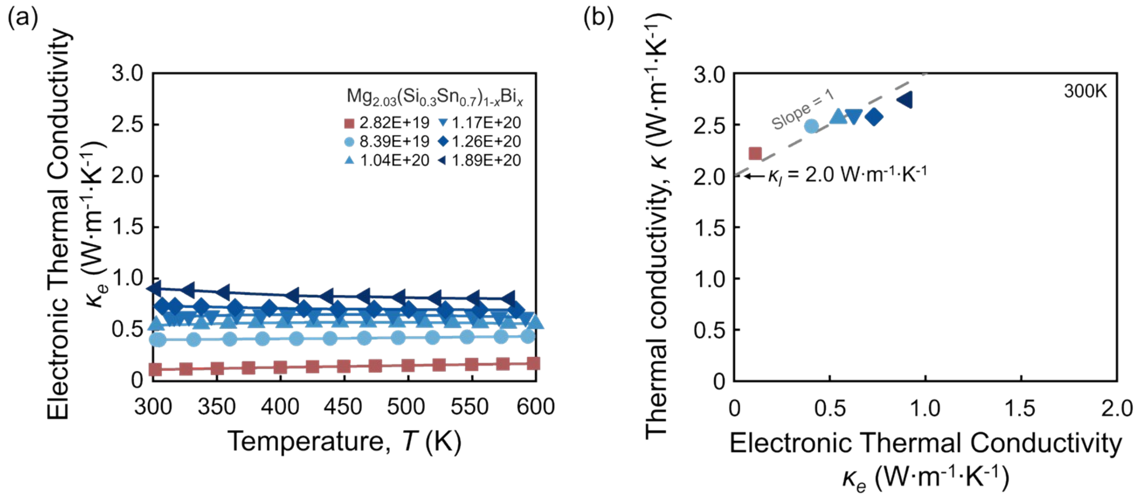

Fig. S5. Estimation of lattice thermal conductivity (κ_L) at 300 K from total thermal conductivity (κ) and electronic thermal conductivity (κ_e). (a) Temperature-dependent κ_e, calculated as $\kappa_e = L(|S|)\sigma T$, where $L(|S|)$ is the Lorenz number expressed as a function of thermopower. (b) κ plotted as a function of κ_e. The dashed line with a slope of one represents the linear relation $\kappa = \kappa_e + \kappa_L$. The y-intercept of this line indicates the estimated κ_L.[3]

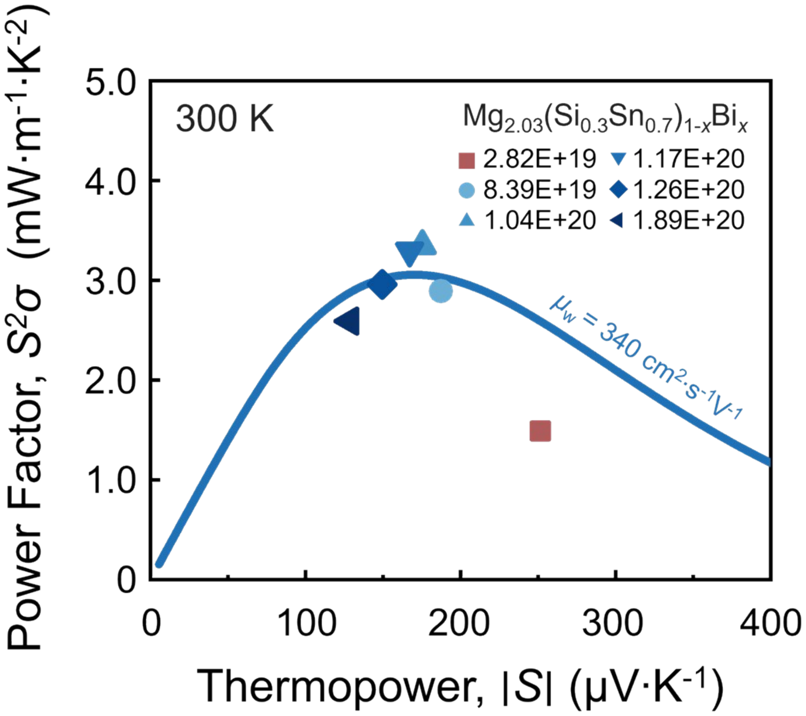

Fig. S6. Impact of weighted mobility (μ_w) on theoretical maximum power factor ($S^2\sigma$). $|S|$-dependent $S^2\sigma$ of Bi-doped $Mg_2Si_{0.3}Sn_{0.7}$ calculated using Eq. 5. Heavily Bi-doped samples (shown in blue) exhibit comparable μ_w values and consequently show no significant change in the theoretical maximum $S^2\sigma$.[3]

Section S4. Quantitative validation of Eq. 7 against Hall measurement-based Effective Mass (EM) model

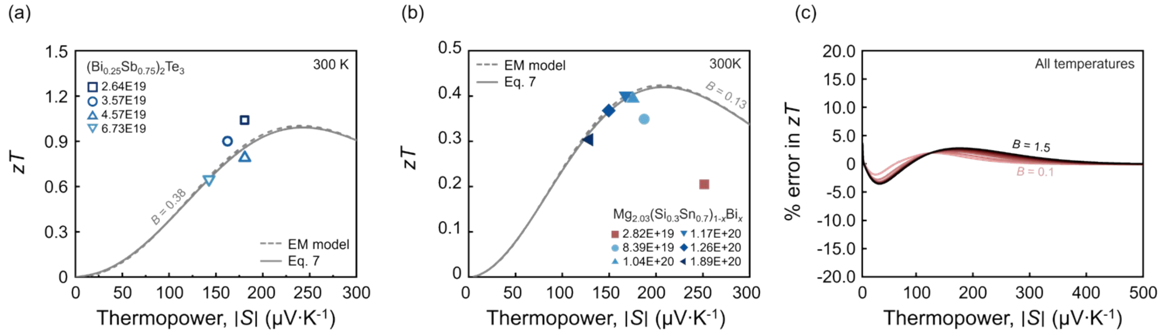

Fig. S7. Validation of Eq. 7 against the Hall carrier concentration-based Effective Mass (EM) model. Comparison of thermopower-dependent *zT* calculated using Eq. 7 and reconstructed using the Hall-based EM model for (a) $(Bi_{0.25}Sb_{0.75})_2Te_3$ and (b) $Mg_{2.03}(Si_{0.3}Sn_{0.7})_{1-x}Bi_x$. (c) Calculated percentage deviation in *zT* predicted by Eq. 7 relative to the Hall-based EM model over a range of thermopower values.

To quantitatively assess the predictive capability of Eq. 7, a direct comparison was performed between zT values calculated using the thermopower-based formulation (Eq. 7) and those reconstructed using a Hall carrier concentration-based Effective Mass (EM) model.

In the EM model calculations, experimentally measured Hall carrier concentrations (n_H) were used to evaluate transport properties within the effective mass formalism. Within this framework, S, σ, and zT are obtained simultaneously as functions of n_H. The resulting n_H-dependent S relationship was then used to convert the n_H-dependent zT into thermopower-dependent form, thereby enabling a direct comparison with Eq. 7, which is inherently formulated as $zT(|S|)$.

Figs. S7(a,b) compare the thermopower-dependent zT curves obtained from the two approaches for representative thermoelectric systems: $(Bi_{0.25}Sb_{0.75})_2Te_3$ and $Mg_{2.03}(Si_{0.3}Sn_{0.7})_{1-x}Bi_x$. For identical thermoelectric quality factor (B) values, the $zT(|S|)$ curves predicted by Eq. 7 closely overlap with those reconstructed using the Hall-based EM model, demonstrating strong quantitative agreement.

To further evaluate predictive accuracy, the percentage deviation between the two methods was calculated as:

$$\Delta zT(\%) = \frac{zT_{Eq.7} - zT_{EM}}{zT_{EM}} \times 100 \qquad \text{(S14)}$$

where $zT_{Eq.7}$ and zT_{EM} are the zT predicted using Eq. 7 and the EM model, respectively.

Fig. S7(c) shows the deviation as a function of thermopower across a range of B values. Because the deviation is plotted explicitly versus $|S|$ rather than temperature, the relevant validity condition is that the evaluated thermopower corresponds to transport regimes dominated by diffusion thermopower, excluding regions where phonon drag or strong bipolar conduction significantly alters transport behavior. Within this physically valid regime, the deviation remains small. Specifically, for $|S| > 100$ μV K^{-1}, the percentage error remains below 3% across all examined B values. At lower thermopower, the maximum deviation approaches ~4% at $B = 1.5$. Even in the case of $B = 1$, where the theoretical maximum zT approaches ~2, the deviation remains below ~4% across the full degeneracy range.

The observed deviation (< 4%) is substantially smaller than typical experimental uncertainties in thermoelectric transport measurements (often ~10–20%), confirming the quantitative robustness of Eq. 7 for performance prediction.

The above comparison clarifies the scope and limitations of Eq. 7 relative to Hall-based EM model analysis. Eq. 7 is formulated for quantitative prediction and optimization of thermoelectric performance. Within this framework, B, theoretical maximum zT (zT_{max}), optimal thermopower for achieving zT_{max}, and μ_{w} can be determined directly from standard thermoelectric measurements (S, σ, κ), without requiring independent n_H measurements. In this performance-oriented context, Hall measurements are not necessary.

However, Eq. 7 should not be interpreted as a replacement for Hall-based electronic band structure analysis. Determination of Seebeck effective mass, construction of Pisarenko relations (S *vs.* n_H), separation of band mass from scattering contributions, and validation of non-parabolic or converged band behavior through n_H-dependent analysis require independent measurement of n_H via the Hall effect. Accordingly, Eq. 7 functions as a Hall-independent performance model and diagnostic transport framework, while remaining complementary to Hall-based methods for rigorous band parameter extraction.

Table S1. Theoretical electrical conductivity (σ) calculation from thermopower ($|S|$) and weighted mobility (μ_w). Calculated σ using Eq. 5 while treating $|S|$ and μ_w as independent variable and fitting parameter, respectively.[3]

Experiment			
Composition	**T (K)**	**S (μV K^{-1})**	**σ (S cm^{-1})**
2.82E+19	300	252	235
8.39E+19	300	187	815
1.04E+20	300	175	1084
1.17E+20	300	167	1189
1.26E+20	300	150	1379
1.89E+20	300	129	1663

Calculated $\lvert S\rvert$-σ curves (Eq. 6)		
Heavily doped samples		
Independent variable	Fitting parameter	Dependent variable
$\lvert S\rvert$ (μV K^{-1})	μ_w (cm^2 V^{-1} s^{-1})	σ (S cm^{-1})
0	340	1133610
50	340	5595
100	340	2520
150	340	1341
200	340	745
250	340	417
300	340	233
350	340	131
400	340	73
Plot in *y*-axis		Plot in *x*-axis

Table S2. Theoretical thermoelectric figure-of-merit (zT) calculation from thermopower ($|S|$) and thermoelectric quality factor (B). Calculated zT using Eq. 7 while treating $|S|$ and B as independent variable and fitting parameter, respectively.[3]

<table>
<tr><th colspan="6">Experiment</th></tr>
<tr><td>Composition</td><td>T (K)</td><td>$|S|$ (μV K^{-1})</td><td>σ (S cm^{-1})</td><td>κ (W m^{-1} K^{-1})</td><td>zT</td></tr>
<tr><td>2.82E+19</td><td>300</td><td>252</td><td>237</td><td>2.2</td><td>0.20</td></tr>
<tr><td>8.39E+19</td><td>300</td><td>187</td><td>815</td><td>2.5</td><td>0.35</td></tr>
<tr><td>1.04E+20</td><td>300</td><td>175</td><td>1084</td><td>2.6</td><td>0.39</td></tr>
<tr><td>1.17E+20</td><td>300</td><td>167</td><td>1189</td><td>2.6</td><td>0.40</td></tr>
<tr><td>1.26E+20</td><td>300</td><td>150</td><td>1379</td><td>2.6</td><td>0.37</td></tr>
<tr><td>1.89E+20</td><td>300</td><td>129</td><td>1663</td><td>2.7</td><td>0.30</td></tr>
<tr><th colspan="6">Calculated $|S|$-zT curves (Eq. (7))</th></tr>
<tr><td colspan="6">Heavily doped samples</td></tr>
<tr><td colspan="2">Independent variable</td><td colspan="2">Fitting parameter</td><td colspan="2">Dependent variable</td></tr>
<tr><td colspan="2">$|S|$ (μV K^{-1})</td><td colspan="2">B</td><td colspan="2">zT</td></tr>
<tr><td colspan="2">0</td><td colspan="2">0.13</td><td colspan="2">0</td></tr>
<tr><td colspan="2">50</td><td colspan="2">0.13</td><td colspan="2">0.08</td></tr>
<tr><td colspan="2">100</td><td colspan="2">0.13</td><td colspan="2">0.24</td></tr>
<tr><td colspan="2">150</td><td colspan="2">0.13</td><td colspan="2">0.37</td></tr>
<tr><td colspan="2">200</td><td colspan="2">0.13</td><td colspan="2">0.42</td></tr>
<tr><td colspan="2">250</td><td colspan="2">0.13</td><td colspan="2">0.40</td></tr>
<tr><td colspan="2">300</td><td colspan="2">0.13</td><td colspan="2">0.34</td></tr>
<tr><td colspan="2">350</td><td colspan="2">0.13</td><td colspan="2">0.26</td></tr>
<tr><td colspan="2">400</td><td colspan="2">0.13</td><td colspan="2">0.20</td></tr>
<tr><td colspan="2">Plot in x-axis</td><td colspan="2"></td><td colspan="2">Plot in y-axis</td></tr>
</table>

Table S3. Theoretical figure-of-merit (*zT*) change with carrier concentration tuning inferred from thermopower (|*S*|) and thermoelectric quality factor (*B*) dependent theoretical maximum *zT* (*zT*$_{max}$). Calculated figure-of-merit (*zT*) in Fig. 1 using Eq. 7 while treating |*S*| and *B* as independent variable and fitting parameter, respectively.

Calculated *B*-dependent |*S*|-*zT* curves (Eq. (7))						
|*S*| (μV K^{-1})	*zT*					
	B = 0.1	*B* = 0.2	*B* = 0.4	*B* = 0.6	*B* = 0.8	*B* = 1.0
100	0.20	0.29	0.37	0.41	0.44	0.45
120	0.25	0.38	0.51	0.58	0.62	0.64
140	0.29	0.46	0.64	0.75	0.81	0.85
160	0.31	0.52	0.77	0.91	1.01	1.07
180	0.33	0.56	0.87	1.06	1.19	1.29
200	0.34	0.59	0.95	1.19	1.36	1.49
220	0.33	0.60	1.00	1.28	1.49	1.65
240	0.32	0.59	1.01	1.33	1.58	1.78
260	0.31	0.57	1.01	1.35	1.62	1.85
280	0.29	0.54	0.97	1.33	1.63	1.88
300	0.26	0.50	0.93	1.29	1.59	1.86
Plot in *x*-axis	Plot in *y*-axis					

Table S4. Theoretical thermopower (|*S*|)-dependent power factor ($S^2\sigma$) and figure-of-merit (*zT*) and experimental data. Calculated thermopower (|*S*|)-dependent power factor ($S^2\sigma$) and figure-of-merit (*zT*) in Fig. 2 using Eq. 6 and 7 at fixed weighted mobility (μ_w = 250 cm^2 V^{-1} s^{-1}) and thermoelectric quality factor (B = 0.25).

Experiment			
Ref. No.	|*S*| (μV K^{-1})	$S^2\sigma$ (mW m^{-1} K^{-2})	*zT*
39	136	2.10	0.43
40	104	1.69	0.30
	114	1.77	0.25
41	112	2.03	0.32
	176	2.70	0.55
	178	2.71	0.56
	211	2.31	0.61
	220	2.25	0.62
42	283	2.05	0.73
	148	2.61	0.68
43	109	2.45	0.37
44	148	2.24	0.75
	135	1.87	0.57
	132	2.00	0.46
45	284	1.44	0.56
	194	1.87	0.56
46	244	2.29	0.68
47	183	2.51	0.71
	181	2.20	0.72
48	105	1.40	0.41
49	219	2.36	0.69
	175	2.26	0.60
50	204	2.37	0.69
51	176	2.14	0.66
	239	1.83	0.70
52	179	2.46	0.63
	175	2.49	0.67
	166	2.23	0.65
	155	2.45	0.61
53	163		0.59

Calculated $|S|$-$S^2\sigma$ and $|S|$-zT curves (Eq. 6 and 7)		
$|S|$ (μV K^{-1})	$S^2\sigma$ (mW m^{-1} K^{-2})	zT
100	1.85	0.32
120	2.05	0.42
140	2.18	0.51
160	2.24	0.59
180	2.24	0.66
200	2.19	0.69
220	2.10	0.71
240	1.98	0.71
260	1.85	0.69
280	1.70	0.66
300	1.54	0.62
Plot in x-axis	Plot in y-axis	

Table S5. Theoretical thermopower (|*S*|)-dependent electrical conductivity (σ) and experimental data. Calculated thermopower (|*S*|)-dependent electrical conductivity (σ) in Fig. 3a using Eq. 6 at fixed weighted mobility values (μ_w = 420 and 670 cm^2 V^{-1} s^{-1} for *p*-Bi_2Te_3 and $(Bi_{0.25}Sb_{0.75})_2Te_3$, respectively).

Experiment			
Ref. No.	Composition	|*S*| (μV K^{-1})	σ (S cm^{-1})
61	*p*-Bi_2Te_3	238	713
62		270	377
63		247	546
64		226	592
		181	1390
		126	2292
		108	2650
		91	3570
		83	3951
65		258	543
66		223	578
		221	592
67		141	1717
68	$(Bi_{0.25}Sb_{0.75})_2Te_3$	162	2280
		157	2450
		181	1885
69		222	1128
70		222	1132

Calculated |*S*|-$S^2\sigma$ and |*S*|-zT curves (Eq. 6 and 7)		
|*S*| (μV K^{-1})	σ (S cm^{-1})	
	μ_w = 420 cm^2 V^{-1} s^{-1}	μ_w = 670 cm^2 V^{-1} s^{-1}
50	6912	11026
100	3113	4967
150	1656	2642
200	921	1469
250	616	822
300	288	460
Plot in *x*-axis	Plot in *y*-axis	

Table S6. Temperature-dependent weighted mobility (μ_w) of experimental data. Temperature (T)-dependent weighted mobility (μ_w) showing effect of grain boundary scattering in $Mg_3(Sb,Bi)_2$ and Nb incorporated $Mg_3(Sb,Bi)_2$.

Experiment				
Ref. No.	Composition	Grain size (μm)	T (K)	μ_w (cm^2 V^{-1} s^{-1})
71	$Mg_3Sb_{1.5}Bi_{0.5}$	~ 1	350	34
			390	49
			440	61
			490	67
			540	67
			590	63
	$Mg_3Sb_{1.5}Bi_{0.5}$	~ 10	320	144
			350	146
			420	127
			490	100
			570	78
	$Mg_3Sb_{1.5}Bi_{0.5}$	~ 30	320	269
			350	218
			390	176
			440	141
			490	114
			540	93
			590	81
72	$Mg_3Sb_{0.3}Bi_{0.7}$ + Nb	~ 10	330	302
			348	265
			373	236
			498	211
			423	188
			448	167
			473	148
			523	113
			573	84

References

1. H. J. Goldsmid, in *Introduction to Thermoelectricity*, ed. H. J. Goldsmid, Springer-Verlag GmbH, Heidelberg, 2016, pp. 45–66.
2. H.-S. Kim, N. A. Heinz, Z. M. Gibbs, Y. Tang, S. D. Kang and G. J. Snyder, *Materials Today*, 2017, **20**, 452–459.
3. K. Cheng, Z. Bu, J. Tang, X. Zhang, X. Meng, W. Li and Y. Pei, *Materials Today Physics*, 2022, **28**, 100887.